NANO · MICRO small
www.small-journal.com

Adaptive Synaptic Memory via Lithium Ion Modulation in RRAM Devices

Chih-Yang Lin, Jia Chen, Po-Hsun Chen, Ting-Chang Chang, Yuting Wu, Jason K. Eshraghian, John Moon, Sangmin Yoo, Yu-Hsun Wang, Wen-Chung Chen, Zhi-Yang Wang, Hui-Chun Huang, Yi Li, Xiangshui Miao, Wei D. Lu, and Simon M. Sze*

Biologically plausible computing systems require fine-grain tuning of analog synaptic characteristics. In this study, lithium-doped silicate resistive random access memory with a titanium nitride (TiN) electrode mimicking biological synapses is demonstrated. Biological plausibility of this RRAM device is thought to occur due to the low ionization energy of lithium ions, which enables controllable forming and filamentary retraction spontaneously or under an applied voltage. The TiN electrode can effectively store lithium ions, a principle widely adopted from battery construction, and allows state-dependent decay to be reliably achieved. As a result, this device offers multi-bit functionality and synaptic plasticity for simulating various strengths in neuronal connections. Both short-term memory and long-term memory are emulated across dynamical timescales. Spike-timing-dependent plasticity and paired-pulse facilitation are also demonstrated. These mechanisms are capable of self-pruning to generate efficient neural networks. Time-dependent resistance decay is observed for different conductance values, which mimics both biological and artificial memory pruning and conforms to the trend of the biological brain that prunes weak synaptic connections. By faithfully emulating learning rules that exist in human's higher cortical areas from STDP to synaptic pruning, the device has the capacity to drive forward the development of highly efficient neuromorphic computing systems.

The biological brain has set a golden standard in computational efficiency, both due to its massive parallelism, and its ability to perform in-memory computing within the same ionic substrate. Ion-gated channels determine synaptic strength which is known to be a mechanism for memory storage, and the very same ions that pass through these gates encode data in the form of spikes. Communication, computation, and storage all occur within the same local medium. The brain's ability to perform in-memory processing within a unified ionic mechanism has driven many researchers to apply ion-driven non-volatile memories to emulate learning rules at the device-level.[1–12]

The operating principles of resistive random access memory (RRAM) draw parallel with biological synapses. From a physical standpoint, the top electrode (TE) corresponds to a pre-synaptic terminal, the insulator layer acts as the substrate through which neurotransmitters are released, and the bottom electrode (BE)

C.-Y. Lin
Department of Physics
National Sun Yat-sen University
No.70 Lien-hai Road, Kaohsiung 80424, Taiwan
J. Chen, Prof. Y. Li, Prof. X. Miao
Wuhan National Laboratory for Optoelectronics
School of Optical and Electronic Information
Huazhong University of Science and Technology
No.1037 Luoyu Road, Wuhan 430074, China
Prof. P.-H. Chen
Department of Applied Science
R.O.C. Naval Academy
No.669 Junxiao Road, Kaohsiung 81345, Taiwan
Prof. P.-H. Chen
Center for Nanoscience and Nanotechnology
National Sun Yat-sen University
No.70 Lien-hai Road, Kaohsiung 80424, Taiwan
The ORCID identification number(s) for the author(s) of this article can be found under https://doi.org/10.1002/smll.202003964.
Prof. T.-C. Chang
Department of Physics
The Center of Crystal Research
National Sun Yat-sen University
No.70 Lien-hai Road, Kaohsiung 80424, Taiwan
E-mail: tcchang3708@gmail.com
Y. Wu, Dr. J. K. Eshraghian, J. Moon, S. Yoo, Prof. W. D. Lu
Electrical Engineering and Computer Science
University of Michigan
No.1301 Beal Avenue, Ann Arbor, Michigan 48109-2122, USA
Y.-H. Wang, Prof. S. M. Sze
Department of Electronics Engineering and Institute of Electronics
National Chiao Tung University
No.1001 University Road, Hsinchu 30010, Taiwan
W.-C. Chen, Z.-Y. Wang, Dr. H.-C. Huang
Department of Materials and Optoelectronic Science
National Sun Yat-sen University
No.70 Lien-hai Road, Kaohsiung 80424, Taiwan

DOI: 10.1002/smll.202003964

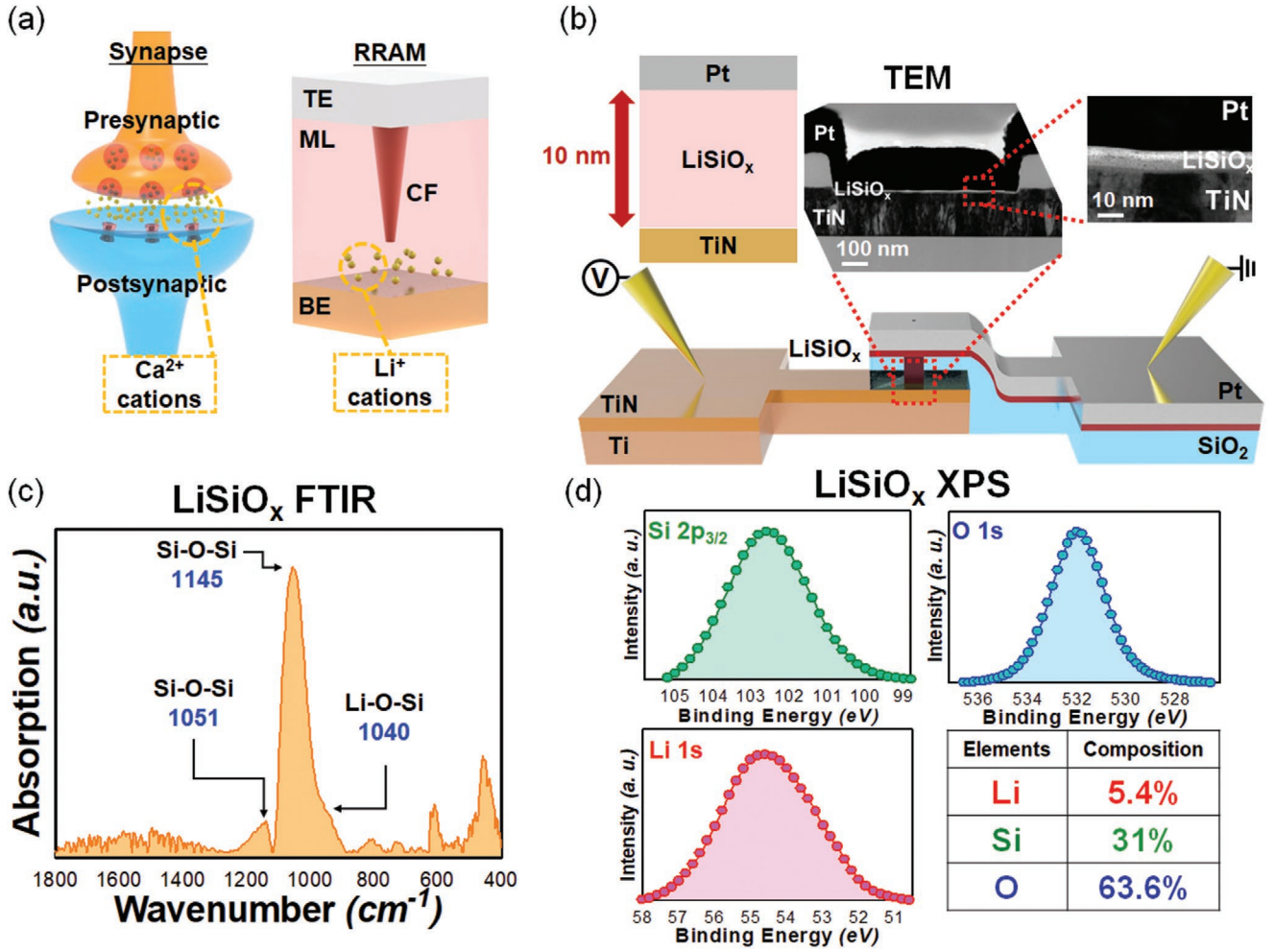

Figure 1. a) 3D schematic structure of both a synapse and the RRAM devices. For the synapse, the calcium cations were generated by the stimulation signals from the neuron to the presynaptic. More cations will increase the synaptic strength, which represents a stronger connection (greater conductance) between a pair of nodes (pre- and post-synaptic terminals). CF refers to the conduction filament and ML is the middle switching layer. The function of lithium cations is similar to calcium cations in a synapse. b) Via-based Pt/LiSiOx/TiN cell with an applied voltage on the TiN BE and TEM images of the switching layer. c,d) Material analysis results. c) FTIR measurement of the LiSiOx middle layer. The Li—O—Si bond is observed at 1040 cm^{-1}; d) XPS measurement results of the LiSiOx middle layer. The proportions of lithium, silicon, and oxygen are 5.4%, 31%, 63.6%, respectively.

acts as the post-synaptic terminal (**Figure 1**a). From a functional perspective, RRAM features low operating voltages, low energy consumption, fast write-erase, high endurance, and a long shelf-life. Between these physical and functional advantages, RRAM has drawn significant academic and industry attention.[13–15]

In this work, we use lithium ions in the switching layer of an RRAM to emulate calcium ion transport at chemical synaptic junctions, and the titanium nitride (TiN) electrode to act as a reservoir for ion storage. In doing so, we demonstrate continuous multi-state synaptic gating which is useful for modeling various connection strengths between nodes in a directed graph.[16,17] In addition to the fine-grain tuning of multi-resistance states, we show that long-term memory (LTM) and short-term memory (STM) can be achieved with time-dependent memory decay, replicating the various orders of magnitude difference of time-scale operation that occurs throughout hierarchical regions of the brain from seconds to days. In doing so, this RRAM device has the capacity to mimic ionic mechanisms in synapses faithfully that enables efficient learning and data processing.[18–24] We also present an empirically-driven conduction-based model of our device.

The detailed fabrication process of lithium silicate ($LiSiO_x$) RRAM using the via hole structure is provided in the experimental section. Figure 1b shows the structure of the fabricated RRAM devices and transmission electron microscopy (TEM) images, where the BE is 200-nm-thick TiN, the middle switching layer is a 10-nm-thick $LiSiO_x$ flake, and finally, a 200-nm-thick platinum (Pt) deposited as the TE. Further detail regarding the manufacturing process flow is provided in Figure S1, Supporting Information. All voltages are applied on the TiN BE, with the Pt TE grounded.

The bond conditions of the device were captured using Fourier-transform infrared spectroscopy (FTIR), shown in Figure 1c, which clearly captures the Li—O—Si bond at 1040 cm^{-1}.[25,26] Figure 1d shows the X-ray photoelectron

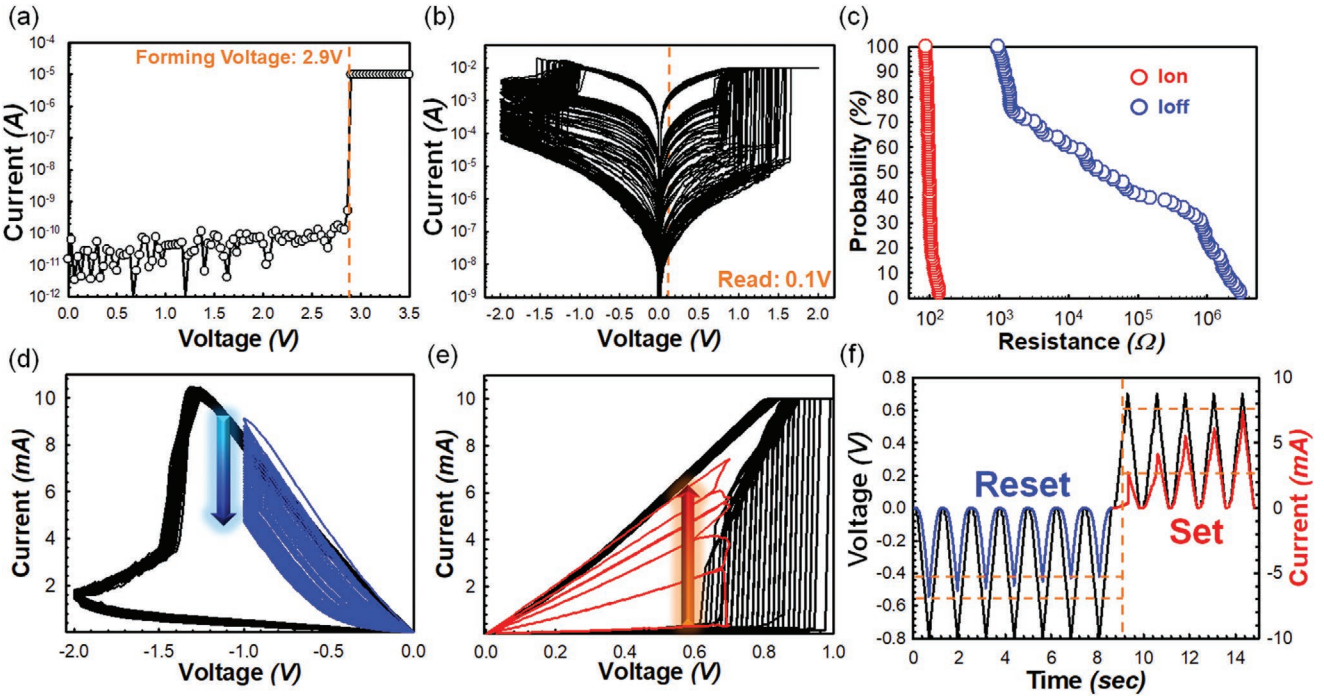

Figure 2. The basic electrical characteristics of a Pt/LiSiOx/TiN device. a) *I–V* sweep of the forming process occurring at 2.9 V. b) *I–V* curve for programming 100 cycles within a peak amplitude of ± 2 V. c) Resistance distribution for both LRS and HRS, where LRS is sufficiently stable, and HRS exhibits a wide resistance distribution. d) Gradual reset process under constant –1 V DC sweep cycles. e) The gradual set process under constant 0.7 V DC sweeps cycles. f) The gradual reset and set processes under AC pulses.

spectrum for the $LiSiO_x$ switching layer. The switching layer composition of the $LiSiO_x$ is lithium (Li): 5.4%, silicon (Si): 31%, and oxygen (O): 63.6%.

Through electrical analysis, the lithium silicate RRAM shows abnormal resistive switching behaviors. In particular, the high resistance states (HRS) are distributed over a wide range. Prior to characterization, a positive bias forming voltage sweep was applied to the BE, with the current-voltage (*I–V*) curve from **Figure 2**a showing that the device formed at –2.9 V. Subsequently, the *I–V* characteristic curves can be observed in Figure 2b by applying 100 set and reset operating cycles with programming voltages of ± 2 V. The cumulative statistics of resistive states are provided in Figure 2c, which highlights the multi-state distribution from 1 kΩ to 1 MΩ when applying a read voltage of 0.1 V. Controlling the stop-voltage enables high-fidelity tuning of the device resistance. During operation, traditional RRAM devices will start to drop from low states to high states when applying a voltage exceeding the reset voltage. Contrastingly, when $LiSiO_x$ RRAM has a stop-voltage applied below the reset voltage, the decrease in current is graduated from a low resistance state (LRS) to a HRS, as shown in Figure 2d. Now considering a set process, the RRAM device will suddenly switch from the HRS to the LRS by applying a voltage higher than the set voltage. Nevertheless, when a subthreshold voltage is applied, the $LiSiO_x$ device will incrementally switch from the HRS to the LRS, similar to the incremental reset case, which is illustrated in Figure 2e. Time-varying set and reset processes are plotted in Figure 2f. The continuous reset and set behaviors of the $LiSiO_x$ device demonstrate that this RRAM can operate under direct current (DC) bias, and also under alternating current (AC) pulse conditions. The wide distribution of the $LiSiO_x$ device can be attributed to the conduction region between the filament and electrode. This filament can be easily dissipated and ions will migrate under an applied voltage, which will cause partial release and drift of lithium ions to the TiN electrode (or filament), in accordance to the direction of the electrical field.[16,17] Therefore, the $LiSiO_x$ RRAM can emulate the seemingly analog properties of synaptic weights by controlling the wide resistance distribution in AC pulses.

Neurons communicate via synapses, and their strengths are modulated based on the sequential order of neuronal activity (**Figure 3**a,b). Spike-timing-dependent plasticity (STDP) is a learning rule which proposes that if two neurons are regularly activated together, the strength of their connection will be increased. STDP further proposes that the connection between the two neurons is dependent on the relative timing of activations from the pre-synapse and post-synapse. This is illustrated in Figure 3c, which fits the relationship between relative spike timing and synaptic strength.[27–30]

In prior studies, RRAM was typically used to simulate STDP behavior using progressive waveforms and different voltage waveforms to increase or decrease the original waveform. Several incremental pulses are applied to the TiN input terminal, with a single voltage pulse at an offset time to the Pt.[31] In the $LiSiO_x$ RRAM device, it bears similarities to the synaptic structure of neurons in the brain, the middle dielectric layer is corresponding to the ion reaction zone in the middle of the synapse. As a result, the wide and controllable over 200 resistance states can store the different memory states under different applied voltage precisely.

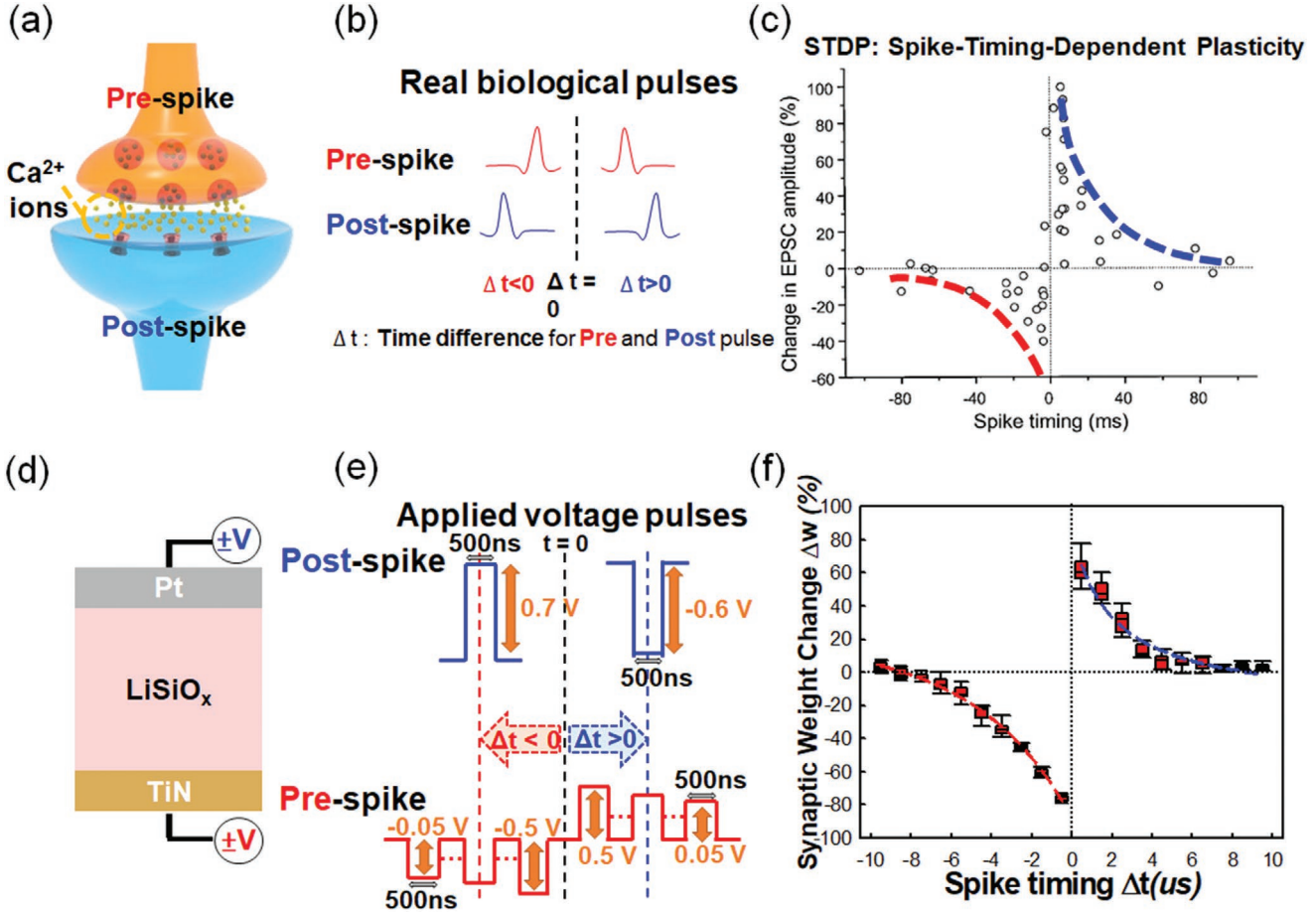

Figure 3. a) Illustration of a chemical synapse. b) Different pre and post spike times for $\Delta t > 0$ and $\Delta t < 0$. c) Experimental STDP curves. An excitatory post-synaptic potential (EPSP) increases the probability of the post-synaptic neuron firing an action potential. The flow of ions that causes an EPSP is an excitatory post-synaptic current. Reproduced with permission,[20] Copyright 1998 Society for Neuroscience. d) The TiN electrode acts as the pre-synaptic terminal; the Pt electrode is the post-synaptic terminal. e) Pulse conditions of both pre-synaptic and post-synaptic terminals. The pre-spike includes incremental negative and decremental positive pulses; the post-spike uses single pulses with negative amplitude for $\Delta t < 0$, and positive amplitude for $\Delta t > 0$. f) Correlation between lithium-based STDP and biological STDP.

To demonstrate STDP, 10 incremental negative voltage pulses are applied to the TiN electrode to perform a reset process. For the set process, 10 decremental voltage pulses are applied. All pulse widths are fixed, and the amplitude is increased as it approaches the midpoint. The voltage input from the Pt electrode is used as a post-synaptic input. By varying the input pulse duration of the post-synaptic terminal, the difference in voltage amplitude is used to program the RRAM devices. The large number of 200 distinguishable states means the differences in voltage amplitude can be fine-tuned to program a different lithium-based synaptic weight. The spike time (Δt) is calculated as the time difference between the midpoints of both pulses applied to the TE and BE. When $\Delta t < 0$, the positive voltage at the Pt electrode enables an incremental reset. In contrast, when $\Delta t > 0$, the negative voltage pulses lead to incrementally setting the device. The specified pulse conditions are shown in Figure 3e. Pulse duration and intervals are 500 ns each. The pre-synaptic pulse amplitudes are a set of 10 incremental pulses from –0.05 to –0.5 V (Δ0.05V) and 10 decremental pulses from 0.5 to 0.05 V(–Δ0.05 V). The post-synaptic pulse is single pulse, with amplitude –0.7 V to reset and 0.6 V to set.

To demonstrate lithium-driven STDP, 20 sets of different spike times were applied which correspond to 10 reset pulses and 10 set pulses. For each time difference between spikes, we repeated the measurement ten times to ensure repeatability. Figure 3f highlights how this device closely resembles STDP characteristics, with variation shown between different trials. The synaptic weight update (Δw) is defined in biology as the change in the synaptic connection between a pair of neurons. Therefore, the pre and post current difference was obtained before and after applying pulses to both TiN and Pt electrodes. The current difference reflects the synaptic strength of RRAM devices, which are the values of the post-synaptic current (I_{post}) and pre-synaptic current (I_{pre}), read out by applying a 0.1 V pulse. The weight update mechanism is expressed in Equation 1.

$$\Delta w = \frac{I_{post} - I_{pre}}{I_{pre}} \times 100\% \quad (1)$$

To test device reliability, the $LiSiO_x$ devices were subjected to high-temperature retention experiments. Various resistive

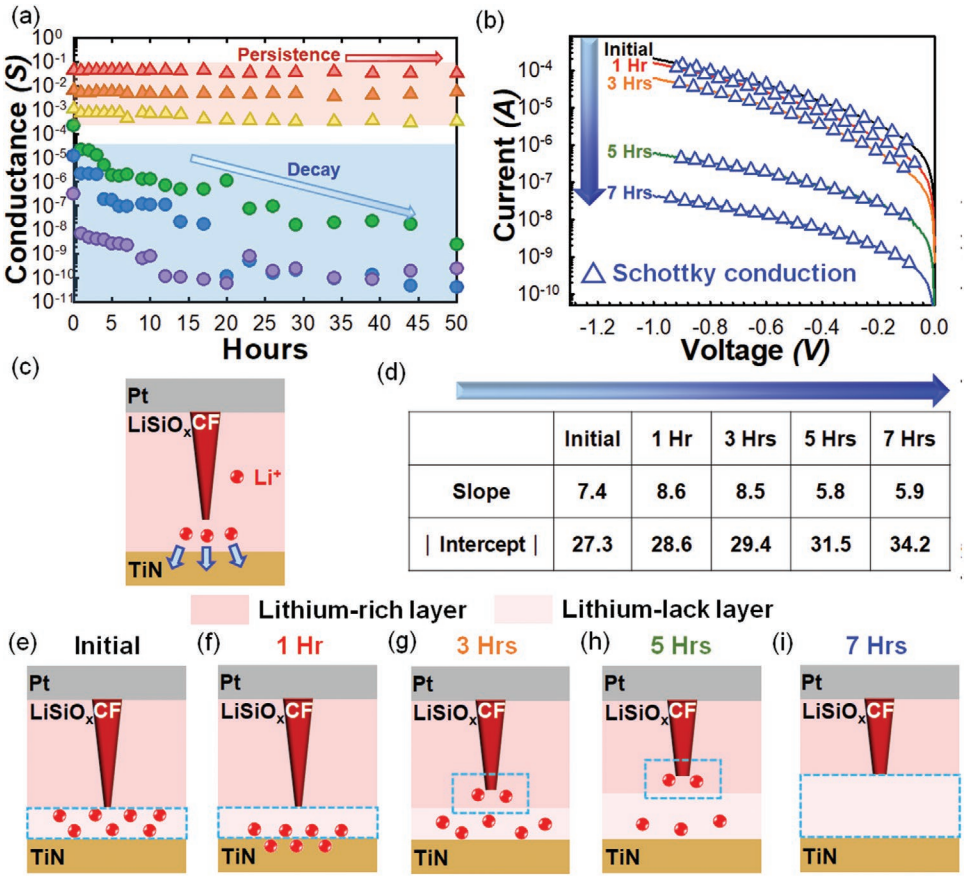

Figure 4. a) Retention results of LiSiOx devices, the different color shading depicts the volatility of this device. The upper section is shaded red, with persistent, non-volatile states; the lower section is shaded blue representing that the states will decay within hours. b) Read current measurements across several hours. c) The natural tendency of the lithium ions to migrate to the TiN electrode. d) Schottky parameter variation over time. e–i) Illustration of the switching mechanism based on the fitting results. The darker red regions represent the higher lithium ions concentration, the lighter red regions represent the lower lithium ions concentration.

states were tested and programmed using a DC sweep. By measuring retention at room temperature over an extended interval time, the time-dependent effects of memory degradation across different states are shown in **Figure 4**a. From the retention characteristics, it can be seen that critical biological features such as STM (shaded blue) and LTM (shaded red) can be natively reproduced at the device level. Based on the corroboration of conduction current fitting analyses, a model is proposed to explain the electrical resistive switching behaviors. An insulator carrier conduction mechanism analysis using current fitting is shown in Figure S3, Supporting Information, which reveals that the components in the conduction mechanism at different times are all Schottky thermal conduction mechanisms, shown in Figure 4b.[32]

From prior literature, TiN, TiO, and TiON are commonly used in the electrodes of lithium batteries, which are excellent storage tanks for lithium ions.[33–35] It is therefore inferred that the lithium ions will naturally migrate to the TiN electrode in the Pt/LiSiO$_x$/TiN device even in the absence of a bias voltage, illustrated in Figure 4c. To draw a conclusion about the conduction mechanism within lithium based devices, the fitting parameters are extracted from the results of the Schottky conduction mechanism at different times. The fitting curves of all Schottky conduction mechanisms and Schottky formulae are shown in Figure S3, Supporting Information. All Schottky parameters, including intercepts and slopes, are listed in Figure 4d. The intercepts represent the conduction barrier heights, and the slopes in the Schottky transmission mechanism are inversely proportional to the square root of the product of dielectric constant and barrier conduction distance. This fitting technique allows us to determine barrier conditions at different times and successfully models lithium-based STM and LTM. The initial state of the device is shown in Figure 4e. The switching layer between the tip and the TiN is composed of lithium-silicide. The lithium ions in the switching layer are then absorbed by the TiN electrode causing the barrier height of the insulator to increase, which simultaneously represents a decrease of the dielectric coefficient as well as an increase of the slope. Next, we compare the parameters after 1 hand 3 h. The different slope decrement for Schottky conduction and the same increment of the intercepts indicate that the lithium ions in the switching layer are increasingly absorbed by the TiN, creating a more insulating lithium silicon layer between the filament tip and the BE. Additionally, the dielectric coefficient decreases along with the slope, which indicates that the filament tip has retracted. Therefore, the electron conduction

distance also increases (Figure 4f,g). The filament tip is affected by the decreased concentration of lithium ions in the switching layer causing the ionization of the filament to move the lithium ions towards the switching layer, which increases electron conduction distance and device resistance.

From three to five hours after programming, the slope of the Schottky conduction mechanism drops dramatically and the intercept increases simultaneously. This indicates that the barrier height has increased and the conduction distance also increases (Figure 4g,h). The lithium filament has retracted more during this time because the lithium ions in the switching layer have almost entirely been absorbed by the TiN electrode. A smaller lithium ion concentration in the switching layer results in the most significant lithium ion concentration gradient, causing the filament to retract. This is the primary cause of the dramatic decrease of the Schottky slope. In the following five to seven hours, the slope of the Schottky conduction mechanism continues to slowly increase, along with the barrier height. The lithium ions in the switching layer are almost entirely absorbed by the TiN electrode (Figure 4h,i).

For commercial-grade devices, we tested the device under a high ambient temperature of 125 °C. Retention was tested on after programming, with readings taken every 500 seconds. A read voltage of −0.1 V is applied to avoid affecting resistive states, followed by a 3-hour warm-up retention test. A total of five different resistance states were tested: one LRS device, and four HRS devices. The HRS devices are denoted HRS1 to HRS4 based on their initial state. An increasing number indicates a higher initial resistance. The current values are used to determine conductance, plotted in Figure 4a and Figure S2, Supporting Information, showing the conductance state remains stable over time in lower resistance states, thus behaving as a reliable long term memory. Interestingly, the retention of HRS devices is not the same. While HRS1 and HRS2 remain unchanged with excellent retention, HRS3 sharply drops by order of 0.5 as measured by the read current. HRS4 decreases sharply even more by a full order of magnitude (Figure S2, Supporting Information).

The time-varying dependence of HRS in this device conforms to the trend that the human brain prunes synaptic connections dependent on memory strength. With the retention results, the volatile characteristics in the HRS can be applied to paired-pulse facilitation (PPF) in a neuron synapse system. PPF is an essential characteristic in memory formation, and is a result of STM synapses which are strongly dependent on calcium ion release.[36–40] PPF is widely applied in several applications such as frequency filters, frequency detectors, sound-source localization, and information processing.[41–44] To demonstrate, spikes are only applied at the pre-synaptic terminal (**Figure 5**a). Figure 5b illustrates the time-dependent calcium ion distribution in the synaptic cleft. For a short time interval, the calcium ions are highly concentrated which corresponds to strengthened

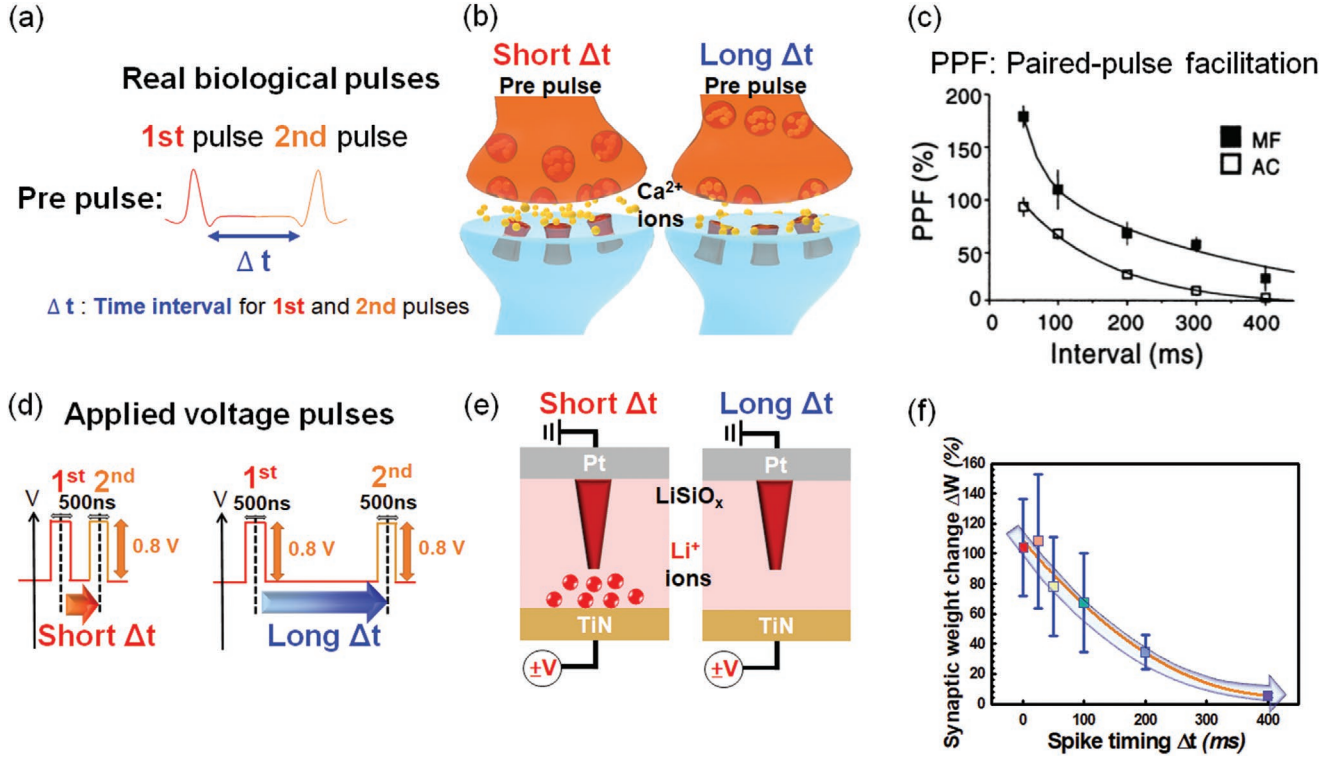

Figure 5. a) Pre-synaptic pulses are applied to the device, where the time between a pair of pulses is the parameter of interest. b) Illustration of a synapse under both STM and LTM. c) PPF curves (Reproduced with permission.[1] Copyright 2020 IEEE). MF is the mossy fiber synapse, AC is assoc/com synapse. d) The input pulse conditions for pre-synaptic spikes, which is designed according to real biological stimuli with two single pulses of identical pulse width (500 ns) and strength (0.8 V) applied to the same electorde. The intervals between two pulses are also designed to correspond to biological spike rates. e) Lithium ion distribution in Pt/LiSiOx/TiN for STM and LTM. f) PPF experimental results were demonstrating a strong degree of biological plausibility for self-pruning.

synaptic connections. In contrast, calcium ions are absorbed over longer interval times which decreases connection strength between neurons. The memory strength will depend on the time interval between input paired pulses as shown in Figure 5c.[45] Our switching mechanism theory suggests this occurs due to the easily dissociated Li conduction filament.

To demonstrate PPF, the voltage pulses are all applied on the TiN BE (Figure 5d). Since this device has multi-state memory, a high voltage amplitude is used to fully reset the device to the highest resistance state prior to taking PPF measurements. For the highest resistance states, a voltage pulse of 0.8 V is insufficient to set the device for LTM retention, but it can apply incremental sets to lower volatile resistance states. By varying the interval time between the two set pulses in Figure 5d, PPF can be realized by using the spike-time difference to alter the lithium-ion concentration in the switching layer (Figure 5e). The detailed pulse conditions and measurements are provided in Figure S4, Supporting Information. Synaptic weight variation results are shown in Figure 5f, as the interval time is varied from 0.1 ms to 400ms, and repeated 20 times to show how the variance of the results can be likened to that of an exponential fit in STDP curves, thus demonstrating the possible use of this device to implement biologically plausible learning rules. Weight changes are achieved by spike-timing variation alone, and the weight difference (Δw) calculation is the same as Equation 1. To examine the device-to-device variability, we use three more samples with identical voltage pulse conditions and present the measurement results in Figure S5, Supporting Information.

In conclusion, dynamical time-varying synaptic characteristics have been demonstrated using $LiSiO_x$ devices, along with the associated switching mechanism. The reservoir of lithium ions gives rise to unique characteristics that approach biologically plausible synaptic behavior, with analog STM and digital LTM for strong connections being realized within the same device. With a wide tuning range of the of HRS, STDP is demonstrated. The volatile properties are leveraged to demonstrate PPF by varying spike-timing, and can be used to build more efficient spiking neural networks that prune weak connections that fall below a given threshold which has already been demonstrated to improve performance and efficiency in conventional neural networks. The proposed lithium-doped RRAM devices show promising results to drive forward the future of complex and dynamical brain-inspired computing.

Experimental Section

Pt/$LiSiO_x$/TiN Device Fabrication: A 200-nm-thick TiN layer was deposited as the BE using chemical vapor deposition on the patterned Ti/SiO_2/Si substrate, and patterned in every single device to obtain excellent device stability and to shrink the device size. SiO_2 was deposited and via hole structure was patterned by the mask aligner process with different hole sizes from 16 um^2 to 0.16 um^2. Next, the photoresist was deposited and exposed to the TE. The isolated switching layer of 10-nm-thick $LiSiO_x$ film was deposited as the insulator by RF sputtering with a $LiSiO_x$ target and an Ar gas flow rate of 30 sccm at a working pressure of 4 mtorr. 200-nm-thick Pt was also deposited using DC sputtering with an Ar gas flow of 30 sccm at a working pressure of 4 mtorr. Finally, the sample was placed in acetone to perform the lift off process and remove the unnecessary parts of the TE.

Device Characterization: The resistive switching behavior and performance were measured using a B1500 and B1505A semiconductor parameter analyzer (Agilent/Keysight) for DC measurement, B1525A for pulse measurements, and B1530A for fast IV measurement (Agilent). The samples were measured using a Cascade Microtech M150 and EPS 150 TESLA (Formfactor). Both DC and AC voltage biases were supplied to the BE (TiN), while the TE (Pt) was grounded. The temperature was controlled by a Lakeshore Model 336 cryogenic temperature controller. Material proportion examination was performed by X-ray photoelectron spectroscopy (XPS), which was measured using a JEOL JAMP-9500F Auger Electron Spectroscopy. The bond composition was confirmed by FTIR, performed with a Bruker VERTEX 70v. Device thickness was measured using the N&K analyzer 1280, and confirmed by TEM. The cross-sectional structure of the Pt/$LiSiO_x$/TiN sample was prepared using a focused ion beam (SEIKO SMI3050SE). Cross-sectional TEM images were obtained using 200kV Tecnai F20 G2 MAT S-TWIN Field Emission Gun Transmission Electron Microscope.

Supporting Information

Supporting Information is available from the Wiley Online Library or from the author.

Acknowledgements

C.-Y.L. and J.C. equally contributed to this work. This work was performed at the Ministry of Science and Technology Core Facilities Laboratory for Nano-Science and Nano-Technology in Kaohsiung-Pingtung. The authors are grateful for the technical support from the focus ion beam engineer, Mr. Yan-Wen Chen, at the Center for Nanoscience and Nanotechnology, National Sun Yat-Sen University. The project was supported by the Ministry of Science and Technology, Taiwan, under Contract No. MOST-108-2917-I-110-001, MOST-108-2823-8-110-001, MOST-108-2811-M-110-516, MOST-108-2218-E-012-001-MY3 and MOST-107-2221-E-009-097-MY2.

Conflict of Interest

The authors declare no conflict of interest.

Keywords

lithium, neuromorphic computing, paired pulse facilitation (PPF), resistive random access memory (RRAM), spike-timing-dependent plasticity (STDP), synaptic plasticity

Received: June 30, 2020
Revised: August 12, 2020
Published online:

[1] X. Y. Zhang, V. Mohan, A. Basu, *IEEE Trans. Circuits Syst.* **2020**, *67*, 816.
[2] J. Koo, J. Kim, S. Ryu, C. Kim, J. J. Kim, *J. Semicond. Tech. Sci.* **2020**, *20*, 195.
[3] M. R. Zhao, B. Gao, J. S. Tang, H. Qian, H. Q. Wu, *Appl. Phys. Rev.* **2020**, *7*, 011301.
[4] L. Sun, G. Hwang, W. Choi, G. Han, Y. Zhang, J. Jiang, S. Zheng, K. Watanabe, T. Taniguchi, M. Zhao, R. Zhao, Y. M. Kim, H. Yang, *Nano Energy* **2020**, *69*, 104472.
[5] H. S. Choi, Y. J. Park, J. H. Lee, Y. Kim, *Electronics* **2020**, *9*, 57.
[6] L. R. Gan, Y. R. Wang, L. Chen, H. Zhu, Q. Q. Sun, *Micromachines* **2019**, *10*, 558.
[7] E. J. Fuller, S. T. Keene, A. Melianas, Z. R. Wang, S. Agarwal, Y. Y. Li, Y. Tuchman, C. D. James, M. J. Marinella, J. J. Yang, A. Salleo, A. A. Talin, *Science* **2019**, *364*, 570.

[8] D. S. Jeong, C. S. Hwang, *Adv. Mater.* **2018**, *30*, 1704729.
[9] C. H. Kim, S. Lim, S. Y. Woo, W. M. Kang, Y. T. Seo, S. T. Lee, S. Lee, D. Kwon, S. Oh, Y. Noh, H. Kim, J. Kim, J. H. Bae, J. H. Lee, *Nanotechnology* **2019**, *30*, 3.
[10] T. H. Lee, D. Loke, K. J. Huang, W. J. Wang, S. R. Elliott, *Adv. Mater.* **2014**, *26*, 7493.
[11] E. Linn, S. Menzel, S. Ferch, R. Waser, *Nanotechnology* **2013**, *24*, 384008.
[12] S. Mandal, A. El-Amin, K. Alexander, B. Rajendran, R. Jha, *Sci. Rep.* **2014**, 4, 5333.
[13] C. Schindler, S. C. P. Thermadam, R. Waser, M. N. Kozicki, *IEEE Trans. Electron Devices* **2007**, *54*, 2762.
[14] M. N. Kozicki, C. Gopalan, M. Balakrishnan, M. Mitkova, *IEEE Trans. Nanotechnol.* **2006**, *5*, 535.
[15] Y. Li, Y. P. Zhong, L. Xu, J. J. Zhang, X. H. Xu, H. J. Sun, X. S. Miao, *Sci. Rep.* **2013**, 3, 1619.
[16] K. C. Chang, T. M. Tsai, T. C. Chang, K. H. Chen, R. Zhang, Z. Y. Wang, J. H. Chen, T. F. Young, M. C. Chen, T. J. Chu, S. Y. Huang, Y. E. Syu, D. H. Bao, S. M. Sze, *IEEE Electron Device Lett.* **2014**, *35*, 530.
[17] J. Chen, C. Y. Lin, Y. Li, C. Qin, K. Lu, J. M. Wang, C. K. Chen, Y. H. He, T. C. Chang, S. M. Sze, X. S. Miao, *IEEE Electron Device Lett.* **2019**, *40*, 542.
[18] S. Deswal, A. Kumar, A. Kumar, *AIP Adv.* **2019**, *9*, 095022.
[19] A. Galves, E. Löcherbach, C. Pouzat, E. Presutti, *J. Stat. Phys.* **2020**, *178*, 869.
[20] H. K. He, R. Yang, H. M. Huang, F. F. Yang, Y. Z. Wu, J. Shaibo, X. Guo, *Nanoscale* **2020**, *12*, 380.
[21] F. Ma, Y. Zhu, Z. Xu, Y. Liu, X. Zheng, S. Ju, Q. Li, Z. Ni, H. Hu, Y. Chai, C. Wu, T. W. Kim, F. Li, *Adv. Funct. Mater.* **2020**, *30*, 11.
[22] M. Salmasi, A. Loebel, S. Glasauer, M. Stemmler, *PLoS Comput. Biol.* **2019**, *15*, e1006666.
[23] Z. Wang, S. Joshi, S. E. Savel'ev, H. Jiang, R. Midya, P. Lin, M. Hu, N. Ge, J. P. Strachan, Z. Li, Q. Wu, M. Barnell, G. L. Li, H. L. Xin, R. S. Williams, Q. Xia, J. J. Yang, *Nat. Mater.* **2017**, *16*, 101.
[24] Z. Wang, R. Yang, H. M. Huang, H. K. He, J. Shaibo, X. Guo, *Adv. Electron. Mater.* **2020**, *6*, 1901290.
[25] M. Q. Snyder, W. J. DeSisto, C. P. Tripp, *Appl. Surf. Sci.* **2007**, *253*, 9336.
[26] N. Yamamoto, H. Takai, *Thin Solid Films* **2000**, *359*, 184.
[27] G. Q. Bi, M. M. Poo, *J. Neurosci.* **1998**, *18*, 10464.
[28] H. Z. Shouval, M. F. Bear, L. N. Cooper, *Proc. Natl. Acad. Sci. U.S.A.* **2002**, *99*, 10831.
[29] M. Graupner, N. Brunel, *Proc. Natl. Acad. Sci. U.S.A.* **2012**, *109*, 21551.
[30] M. C. W. van Rossum, G. Q. Bi, G. G. Turrigiano, *J. Neurosci.* **2000**, *20*, 8812.
[31] D. Kuzum, R. G. D. Jeyasingh, B. Lee, H. S. P. Wong, *Nano Lett.* **2012**, *12*, 2179.
[32] S. M. Sze, *Curr. Contents/Eng. Technol. Appl. Sci.* **1982**, *27*, 28.
[33] Y. C. Qiu, K. Y. Yan, S. H. Yang, L. M. Jin, H. Deng, W. S. Li, *ACS Nano* **2010**, *4*, 6515.
[34] M. Q. Snyder, S. A. Trebukhova, B. Ravdel, M. C. Wheeler, J. DiCarlo, C. P. Tripp, W. J. DeSisto, *J. Power Sources* **2007**, *165*, 379.
[35] Y. H. Yue, P. X. Han, X. He, K. J. Zhang, Z. H. Liu, C. J. Zhang, S. M. Dong, L. Gu, G. L. Cui, *J. Mater. Chem.* **2012**, *22*, 4938.
[36] R. S. Zucker, *Annu. Rev. Neurosci.* **1989**, *12*, 13.
[37] J. Delcastillo, B. Katz, *J. Physiol.* **1954**, *124*, 574.
[38] J. H. Xu, L. M. He, L. G. Wu, *Curr. Opin. Neurobiol.* **2007**, *17*, 352.
[39] F. Diaz-Rojas, T. Sakaba, S. Kawaguchi, *J. Physiol.* **2015**, *593*, 4889.
[40] S. A. Prescott, *Learn. Mem.* **1998**, *5*, 446.
[41] E. S. Fortune, G. J. Rose, *Trends Neurosci.* **2001**, *24*, 381.
[42] L. F. Abbott, W. G. Regehr, *Nature* **2004**, *431*, 796.
[43] K. M. MacLeod, *Hear. Res.* **2011**, *279*, 13.
[44] K. MacLeod, G. Ashida, C. Glaze, C. Carr, in *The Neurophysiological Bases of Auditory Perception* (Eds. E. A. Lopez-Poveda, A. R. Palmer, R. Meddis), Springer, New York, **2010**, 347.
[45] P. A. Salin, M. Scanziani, R. C. Malenka, R. A. Nicoll, *Proc. Natl. Acad. Sci. U.S.A.* **1996**, *93*, 13304.